Thermochemical cycles over redox structured reactors

CrossMark

S. Lorentzou [a,*], C. Pagkoura [a], A. Zygogianni [a], G. Karagiannakis [a],
A.G. Konstandopoulos [a,b,**]

[a] Aerosol & Particle Technology Laboratory, Chem. Process & Energy Resources Inst., Center for Research &
Techn.-Hellas (APTL/CERTH/CPERI), 6th klm. Charilaou-Thermi Rd, P.O. Box 361, 57001, Thessaloniki, Greece
[b] Aristotle Univ. of Thessaloniki, Univ. Campus, 54124, Thessaloniki, Greece

ARTICLE INFO

ABSTRACT

Structured bodies from redox materials are a key element for the implementation of thermochemical cycles on suitable reactors for the solar H_2O splitting. In the current work different configurations of nickel ferrite were investigated with respect to their performance in H_2O splitting: i) powder, ii) disk, iii) honeycomb flow-through monoliths. The structured bodies were prepared via pressing and extrusion techniques. The performance of the different structures was affected significantly by differences in the structural characteristics. Alternative approaches involving casting techniques for the structuring of nickel ferrite porous bodies were also investigated. This work constitutes a preliminary attempt towards tuning such characteristics to achieve enhanced and cycle-to-cycle stable production yields.

© 2017 Hydrogen Energy Publications LLC. Published by Elsevier Ltd. All rights reserved.

Introduction

Although the market is getting progressively open in "structuring" and establishing the set-up towards a hydrogen economy (e.g. realization of hydrogen vehicles and increase in the number of refueling stations), there is still much distance to be covered until all conditions are met for supporting a completely renewable hydrogen production and a relevant infrastructure.

The idea of exploiting solar energy for the implementation of thermochemical cycles for the production of hydrogen from the splitting of H_2O, is intensely investigated during the last years. Thermochemical cycles for hydrogen production via H_2O splitting can offer a practical solution to the very high temperature (typically > 2000 °C) of direct thermolysis reaction schemes. Numerous such cycles have been proposed [1–3], several have been reviewed and investigated [4–7] and the ones currently receiving the highest attention from the research community include sulfur-based cycles, the copper-chlorine, the zinc/zinc oxide system as well as two-step redox stoichiometric and non-stoichiometric cycles of single or mixed metal oxides. Despite operating at substantially lower temperatures in comparison to direct thermolysis reactions,

most of such cycles still require elevated temperatures that can be achieved via technologies exploiting concentrated solar radiation. Solar tower and/or solar dish technologies are capable of meeting the requirements for driving such reactions. Solar energy exploitation enhances further the renewability of those reaction schemes. Exploitation of suitable metal oxides (typically, zinc oxide, iron oxides, ferrites, ceria-based and perovskite compositions), based on stoichiometric and non-stoichiometric thermochemical cycles [8−17], have been acknowledged as having the potential to convert/store solar energy into valuable chemicals. Stoichiometric approaches (i.e. reduction of all the metal cations of a metal oxide to a lower oxidation state, e.g. Fe_3O_4 to FeO), despite of somewhat higher theoretical efficiency, are currently facing the challenge of cyclic structural transitions and phase changes involved, which can result to notable challenges with consequent adverse effects on technical feasibility and long term stability of active materials. The general scheme of non-stoichiometric thermochemical cycles for H_2 production can be written as:

$$M_{x1}N_{x2}O_y \leftrightarrows M_{x1}N_{x2}O_{y-\delta1} + \delta_1/2O_2 \quad (1100 - 1500\,°C) \qquad (1)$$

$$M_{x1}N_{x2}O_{y-\delta1} + \delta_2H_2O \leftrightarrows M_{x1}N_{x2}O_{y-\delta1+\delta2} + \delta_2H_2 \quad (800 - 1200\,°C) \qquad (2)$$
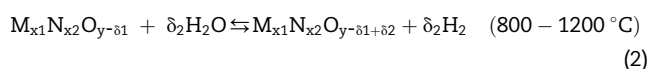
where δ_1, δ_2 represent oxygen deficiencies referring to the thermal reduction step (δ_1) and the material after oxidation by H_2O (δ_2) respectively; M: metal; N: metal and $M_{x1}N_{x2}O_y$ typically corresponding to ferrite (e.g. $NiFe_2O_4$), ceria-based (e.g. $Ce_xZr_{1-x}O_2$) or perovskite (e.g $La_{1-x}Sr_xFeO_3$) structures.

A widely studied concept for the implementation of such cycles on solar reactors relates to structured bodies assemblies [16−25]. Such an approach is simple and in-principle capable of ensuring overall system durability in the course of hundreds of cycles. Such advantages are to some extent at the expense of heat recuperation, however the latter disadvantage can be mitigated significantly via careful overall optimized process design.

Key element of the structured reactors is the substrate, i.e. the inert structure that will accommodate the active materials. However, elimination of interactions of the substrate with the active redox material is quite challenging, especially at the elevated temperatures that are required by the above mentioned solar thermochemical reactions. Naturally, structured bodies shaped entirely from the active redox materials should provide, theoretically, an effective solution to this challenge. Yet, they should be designed to also ensure high gas-solid contact area, robustness and resistance to sintering phenomena induced by high temperatures especially in the course of multiple cycles. Currently the structured reactors are the only ones that have been scaled up to several dozens of kWs (100−750 kW level) [20,25,26].

The present study is an investigation of various structured morphologies based on nickel ferrite, prepared by different shaping techniques. Nickel ferrite was selected for the manufacturing of monolithic structures mainly because of the lower temperature that is required during the thermal reduction step compared for example to CeO_2-based structures, which have been previously materialized and tested for

the same application [16,17], and require temperatures higher than 1500 °C to achieve significant reduction and consequently splitting activity. In addition, the color of Ni-ferrite (black) is most appropriate for structures that are developed as active components of solar absorbers, since it is expected that it will enhance the absorption of solar radiation compared to other lighter colored materials.

The whole development path is presented and the most promising approach is defined outlining further future optimization studies. Long-term exposure results are also presented.

Experimental−methods

Synthesis of redox material

The redox material selected for the development of porous ceramic structures was the $NiFe_2O_4$, which is a well-known and widely investigated composition [12,14,21,27,28]. $NiFe_2O_4$ has also been investigated via computational chemistry (DFT calculations, [29]) where it was shown that it is one of the state-of-the-art formulations in the family of ferrite materials. The nickel ferrite powder was synthesized via the Self-propagating High-temperature Synthesis (SHS) technique from a mixture of Fe, NiO and Fe_2O_3, according to the following reaction scheme:

$$Fe + NiO + 0.5\,Fe_2O_3 + (1.5/4)\,NaClO_4 \rightarrow (NiO)_{1.0}Fe_{2.0}O_3 + (1.5/4)\,NaCl \qquad (3)$$
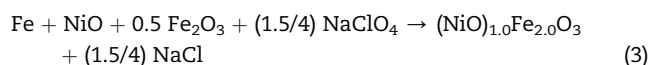
Details on the SHS technique can be found in Refs. [18,30].

Another synthesis route that was applied was the conventional solid state synthesis (SSS), where the raw oxide precursors (i.e. NiO and Fe_2O_3 at the appropriate ratio for the synthesis of nickel ferrite) were well homogenized into a mixture and calcined at 1400 °C to facilitate the formation of the ferrite.

Structuring into porous bodies

Two different structures were prepared; a porous disk geometry and a honeycomb monolithic geometry. Both structures consisted entirely of nickel ferrite. The disk geometry was prepared in order to have a porous structured body that is an intermediate step between the completely loose form of the powder and the well-organized form of a honeycomb monolith. For the preparation of the porous disk a mixture of nickel ferrite with a pore forming agent (i.e. an organic compound) was adequately pressed with the aid of a single-axis hydraulic press to form a dense disk that was further processed to achieve a degree of porosity according to the procedure followed in Refs. [31,32]. Extrusion of honeycomb structures is a process that is performed commercially for the manufacturing of numerous technical ceramics from different materials (e.g. Cordierite, SiC, Al_2O_3 etc) and for a variety of applications, most commonly involving water purification or automotive emission control. Ferrite materials are industrially shaped into structures like toroids, cylinders, tiles

etc., for magnetic applications, while Fe_2O_3 was extruded into honeycomb monolithic segments for catalytic applications in the dehydrogenation of ethylbenzene to styrene [33]. Yet, to the best of our knowledge, this work is the first one reporting the manufacturing of nickel ferrite honeycomb structures via extrusion. The main details of the extrusion process were similar to the ones provided in Refs. [34,35]. Two different "feeding pastes" were extruded in this study; one comprising a stoichiometric mixture of raw oxide reactants (i.e. Fe_2O_3 and NiO) while the other was a nickel ferrite powder prepared via the SHS-synthesis route. Monoliths with varying geometric characteristics were prepared (i.e. different cell density (cells per in^2, cpsi) and wall thickness).

An additional approach applied for the structuring of nickel ferrite into a monolithic body related to specially fabricated molds, using 3D-printing technology, which were used for casting SHS synthesized nickel ferrite into a honeycomb monolithic structure.

The nickel ferrite was evaluated with respect to its H_2O splitting activity in three scales: i) particles in powder form, ii) porous disk, iii) monolith. In all cases the "common denominator" is that the samples consist of the same material formulation (nickel ferrite) and do not contain any additional material (e.g. a ceramic substrate that is coated with the redox material).

Characterization techniques

X-Ray Diffraction analysis (XRD/Siemens D500/501 diffractometer using Cu Kα radiation, λ = 1.5406 Å) was used for the characterization of the phase composition of the samples before and after redox activity assessment. Morphological observations were conducted via an optical microscope (Nikon Stereoscopic Microscope SMZ445) equipped with a Motic Image Plus 3 camera, while Scanning Electron Microscopy (SEM/JEOL 6300) was employed for morphological characterization at higher magnifications. The particle size distribution of the powder samples was measured via a Low Angle Laser Light Scattering Analyzer (LALLS, Malvern Mastersizer-S and Mastersizer 2000). The specific surface area of the materials was characterized via gas adsorption based on the Brunauer–Emmett–Teller (BET) method (TriStar 3000 V6.04 A instrument). Prior to the actual measurements, the samples were degassed at 250 °C overnight in the degassing port. In addition, Hg porosimetry (Autopore 9500, Micromeritics) was also used complementary to the gas adsorption measurement to cover a wider range of pore sizes.

Evaluation of redox activity

All samples, prior to their redox activity assessment, were calcined at 1400 °C under air to attain their fully oxidized form and to deliberately pre-expose them at the upper threshold of the thermal reduction step. This is standard practice to verify stability of the formulations and to minimize high temperature-induced properties' change and subsequent performance variations induced by such phenomena within the temperature range of the subsequent cyclic thermochemical operation (e.g. sintering, surface area loss, phase segregation etc).

The evaluation of the prepared structured bodies' performance with respect to their redox activity in H_2O splitting thermochemical cycles was performed in a dedicated laboratory test rig consisting of a 28-mm-diameter dense alumina tubular reactor enclosed within a high-temperature programmable furnace capable of reaching temperatures up to 1650 °C. All samples were evaluated under the same protocol. The first step was the thermal activation, during which a N_2 flow passed through the fixed bed. Temperature was increased from ambient to 1400 °C with a heating rate of 15 °C/min. Initially, an isothermal step follows at 1400 °C for 1 h under N_2. This step was conducted only once for each material and served the role of evacuating all possible sites from the oxygen contained in the initial state of the fully oxidized material at the specific time scale of 1 h. For the evaluation of the redox activity of the materials, the temperature was reduced to 1100 °C where the oxidation reaction (H_2O splitting) step took place. The duration of the splitting step was 30 min and H_2O concentration in N_2 was varied between two values (low value: 8% and high value 60%). A heated pressurized water tank was employed to achieve the targeted steam concentrations. The oxidation reaction was followed by a 30 min thermal reduction step at 1400 °C. The products of the reaction, after passing through a water trap, were analyzed with the aid of a mass spectrometer (Pfeiffer Omnistar Quadruple Mass Spectrometer). A multi-cyclic experiment involved repetition of the oxidation and thermal reduction steps.

Results–discussion

Ni-ferrite material synthesis

The Ni-ferrite powders were subjected to XRD analysis (Fig. 1) and the observed peaks at (111), (220), (311), (222), (400), (422),
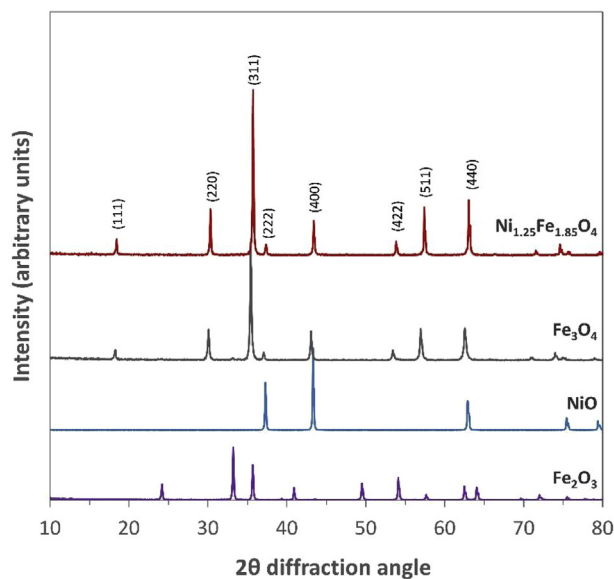
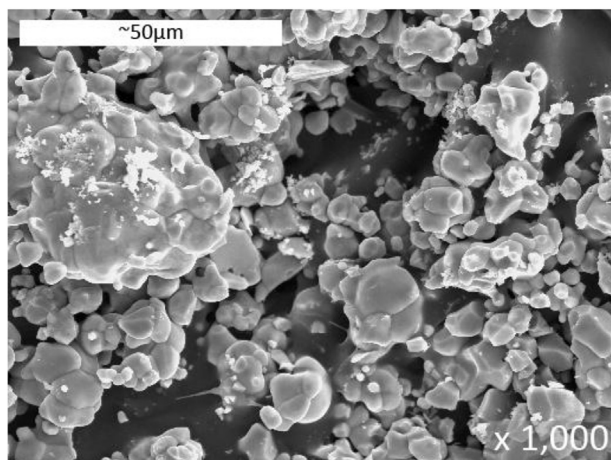**Fig. 1 – XRD spectra of Ni-ferrite synthesized via SHS and of the corresponding precursor oxides.**

Fig. 2 – SEM image of typical irregular shaped particles of SHS produced Ni-ferrite material after high temperature calcination.

Fig. 4 – Ni-ferrite porous disk.

(511), and (440) correspond to the main diffraction planes of the well crystallized fcc nickel ferrite phase. There is no indication of other phases attributed to remnants of the precursors from the synthesis process. However, there is a deviation from the stoichiometric $NiFe_2O_4$ that was expected to be produced based on the precise ratios of the precursors used for the synthesis of the formulation. The identified structure corresponded to $Ni_{1.25}Fe_{1.85}O_4$ (XRD card number 01-088-0380), revealing a rich in Ni product, with no indication, however, of any segregated phase.

After calcination the material suffered from significant sintering (Fig. 2). Originally, the as-synthesized powder had low BET surface area (1.2 m^2/g) measured via gas absorption, which, as expected, decreases to even lower values (~0.3 m^2/g) after calcination at 1400 °C.

Particle size distribution measurements of the as-synthesized material showed a wide size distribution with multiple populations of particles with diameters ranging from under 1 μm up to several hundreds of micrometers. This wide size distribution is an undesirable characteristic of a powder to be used as a raw material for the manufacturing of structured bodies. When the as-synthesized product was further ground via wet ball milling to decrease the particle size and produce a narrower distribution. Indeed, the milling shifted the particle size distribution curve to smaller diameters (curve marked with solid square ■), while relatively large particles (>10 μm) were almost eliminated (Fig. 3).

However, as mentioned in the experimental section, the calcination of the redox material at 1400 °C is performed before assessing its redox activity, which has as a result
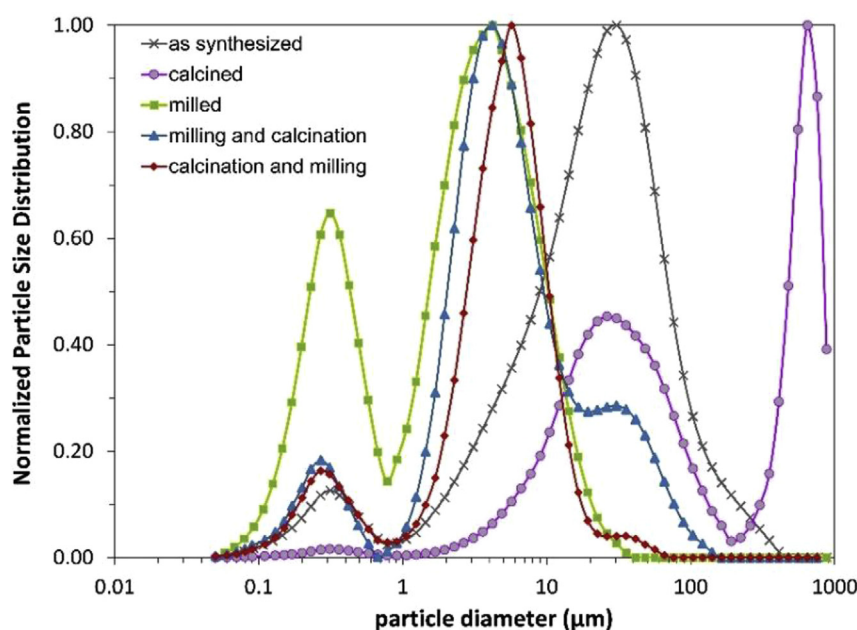

Fig. 3 – Effect of calcination and milling on the particle size distribution of the Ni-ferrite material.
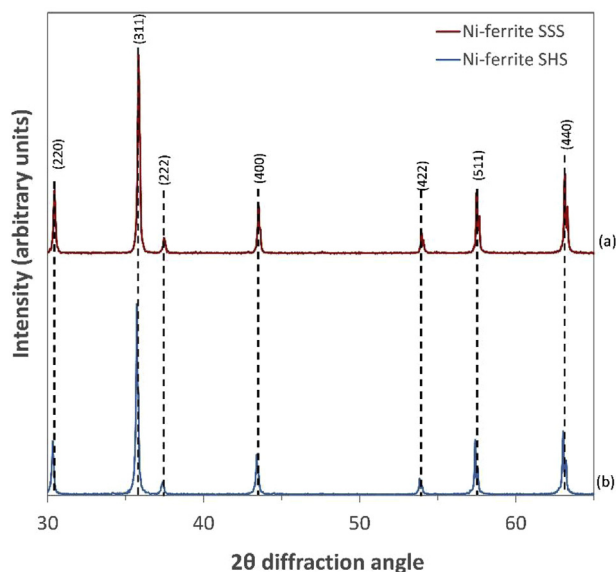
Fig. 5 – Phase composition of the Ni-ferrite monoliths extruded from (a) raw precursors (denoted as "Ni-ferrite SSS") and (b) SHS synthesized Ni-ferrite powder (denoted as "Ni-ferrite SHS").

further increase of the particle size due to sintering (curve marked with solid circle ●). Calcining of the milled product at high temperatures had as a consequence sintering of the milled material and increase of the size of the particles, with an additional third population appearing above 10 μm in the particle size distribution curve (curve marked with solid triangle ▲). Nevertheless, no peak at sizes >200 μm was present in the sample, compared to the case of the as-synthesized-calcined material. Performing the calcination of the as-synthesized material prior to milling and then grinding the calcined product improves the result (curve marked with solid diamond ◆). Therefore, the latter procedure was followed for the preparation of the redox powder for the manufacturing of the porous structures.

Ni-ferrite structured bodies

Porous disk

Ni-ferrite powder (calcined and milled as described earlier) was used for the formation of porous disks (Fig. 4) according to the process described in Refs. [31,32]. The porosity of the structure is a result of the addition of 75% v/v carbon granules (ø1 mm and 2–3 mm length) based on the volume of Ni-ferrite powder (Fig. 4).
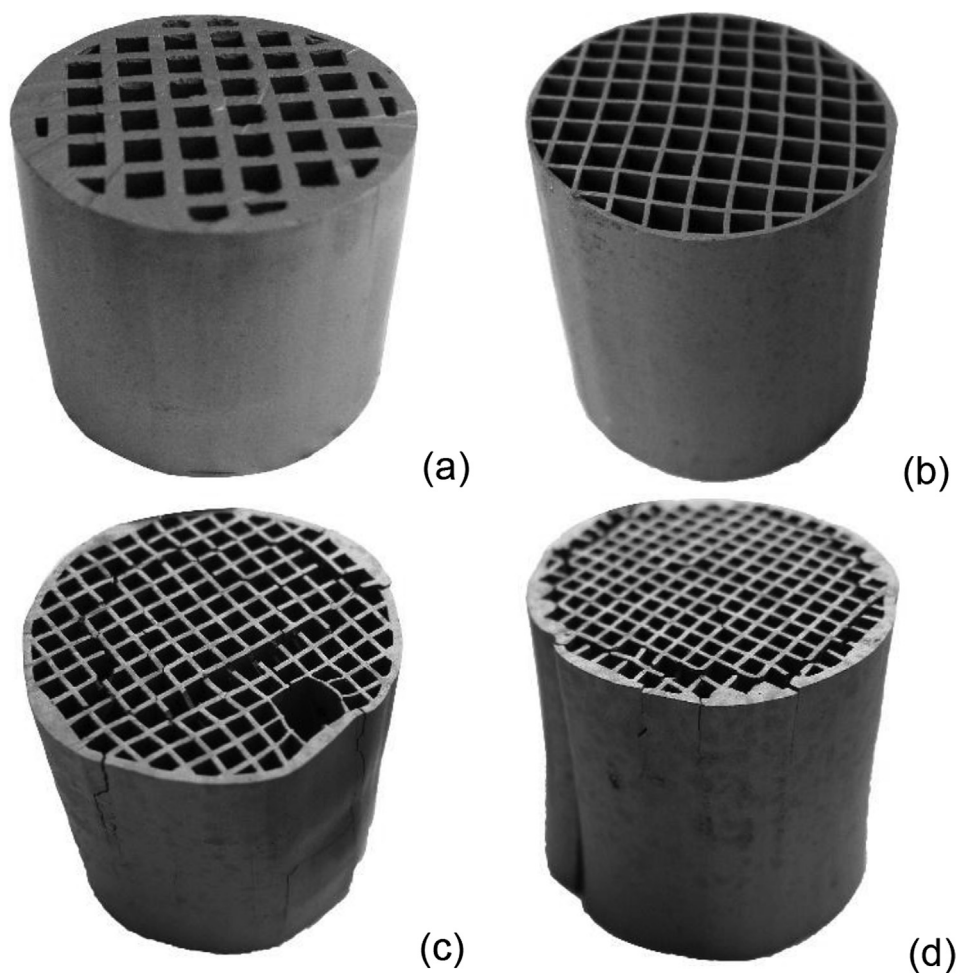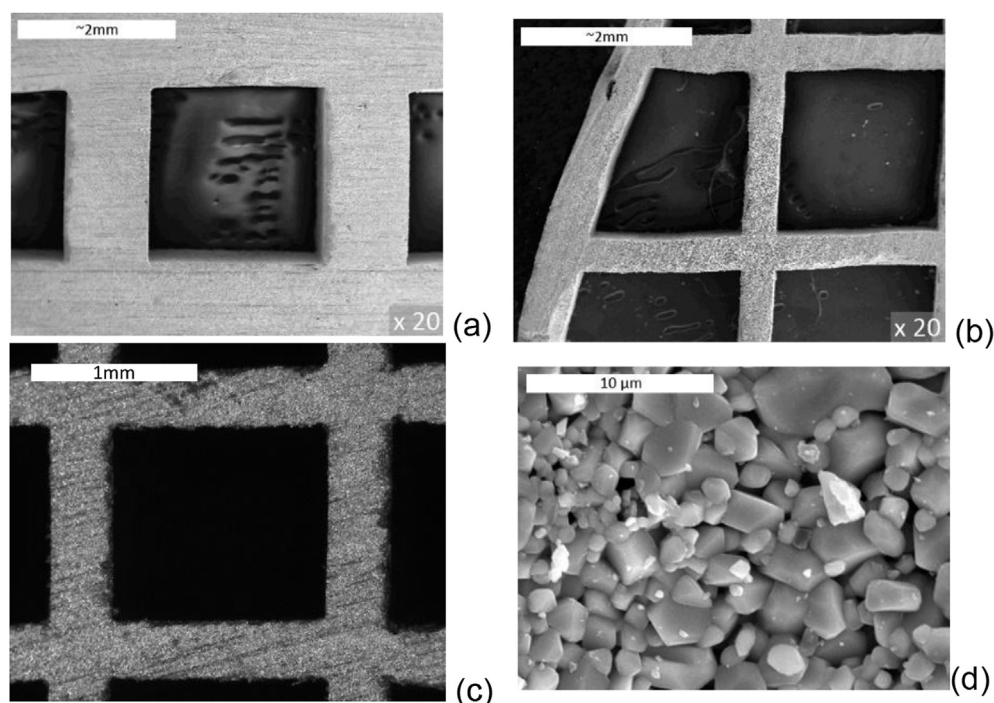

Fig. 6 – Extruded Ni-ferrite monoliths (a) 47 cpsi with 1.2 mm wall thickness, (b) 90 cpsi with 0.47 mm wall thickness, (c) 150 cpsi with 0.47 mm wall thickness and (d) 200 cpsi with 0.47 mm wall thickness.

Table 1 — Main nominal geometrical characteristics of the extrusion dies employed, for the extrusion of NiFe$_2$O$_4$ redox powders.

Structure code	Nominal cell density (cpsi)	Nominal wall thickness (mm)	Nominal channel size (mm)	Nominal surface area (mm^2/mm)
M1-1	47	1.20	2.5	407
M2-1	90	0.47	2.5	690
M2-2	150	0.47	1.6	1045
M2-3	200	0.47	1.3	1160

Fig. 7 — (a) 47 cpsi honeycomb monolith (thick walls), (b) 90 cpsi honeycomb monolith (thin walls), and (c) 150 cpsi honeycomb monolith (thin walls); (d) picture of the wall structure in detail via Scanning Electron Microscopy (SEM).

Honeycomb monoliths via extrusion

Contrary to the porous disk manufacturing, that requires few grams of redox material, the structuring of the ferrite into a honeycomb monolith via a piston extruder requires high amounts of material (in the order of a few kg as a minimum quantity). To this respect, two cases were investigated for the manufacturing of honeycomb extruded monoliths consisting entirely of the redox material. In the first case the raw material that was used was the SHS synthesized Ni-ferrite, while in the second case SSS synthesized Ni-ferrite (described earlier in Section Synthesis of redox material) was employed. The phase composition of the final structure was identical to that of the Ni-ferrite synthesized via SHS (Fig. 5).

Four different structures were manufactured employing different extrusion dies (Fig. 6). The main differences among the four monoliths relate to the wall thickness and the number of channels or channel concentration (cpsi), the nominal geometrical characteristics for each structure (based on the extrusion die) as listed in Table 1. The channel concentration — under the condition that the wall thickness is maintained fixed — is directly related to what is known as "filtration area", or in other words the surface that is directly exposed to the

reactant stream. To achieve high channel concentration, usually, low wall thickness and channel size values are required. The thinner the wall thickness e the more susceptible the structure to thermo-mechanical stresses induced by
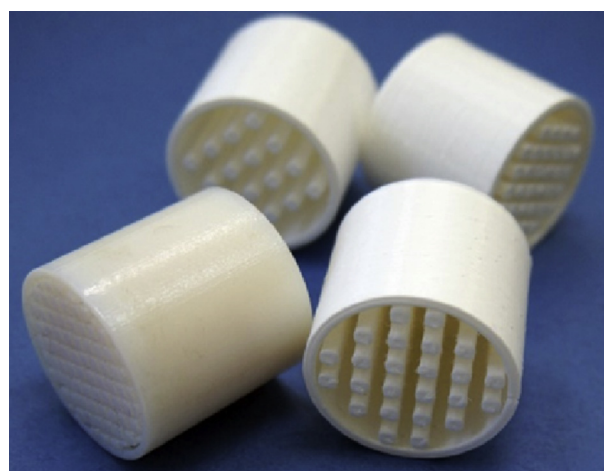

Fig. 8 — Examples of honeycomb type 3D-printed molds.

Table 2 – Structuring of monoliths via 3D-printed molds.

Structure code	Raw material	Particle diameter (μm)	Casting mixture	
3D-1	Ni-ferrite SHS synthesized powder	4.6	Ni-ferrite + H_2O + dispersant + binder	Slurry
3D-2		4.6	Ni-ferrite + H_2O + carbon granules	Paste
3D-3.		28.3	Ni-ferrite + H_2O	Paste

cyclic reactions at high temperatures. Therefore, initially the monolith with the higher wall thickness (1.2 mm) and low active surface (47 cpsi) was chosen. However, it was proven that also the monoliths with the thinner walls had sufficient structural stability, thereby allowing further evaluation for their redox activity. SEM images of the microstructure of the monoliths revealed the grained morphology of the channel wall that was maintained in all cases. The size of the grains (Fig. 7) was in the same order of magnitude with that of the Ni-ferrite powder synthesized via SHS (Fig. 2).

Honeycomb monoliths via casting
Another option for structuring monolithic bodies consisting entirely of the Ni-ferrite was the casting method using molds as sacrificial fugitives. This approach has similarities with the concept of the polyurethane matrices used for the construction of ceramic foams, to create the highly porous monolithic structure. Those molds (Fig. 8) were prepared via a 3D-printing process using the negative template of a honeycomb monolith with square channels. The advantage of this technique compared to the extrusion process for the shaping of redox monolithic structures is that it is more flexible in terms of alterations in geometrical characteristics and does not require massive and expensive equipment (i.e. extruder, extrusion dies, etc). The disadvantage is that, like all methods that involve sacrificial fugitives in the manufacturing process, it has an additional carbon footprint compared to the extrusion process, which, however, will not be quantified in the current work.

Three different monoliths were prepared starting from Ni-ferrite SHS synthesized material. The main characteristics of the three different samples (denoted as 3D-1, 3D-2 and 3D-3) are shown in Table 2.

In the case of 3D-1 and 3D-2, the precursor powder was the SHS synthesized Ni-ferrite that was at a first step fired at 1400 °C and then milled to reduce its particle size distribution (as described in a previous paragraph). This was done in order to formulate structures from the same starting material as the one used in the extruded structures analyzed earlier in the text. A slurry formulation was used for the shaping of the 3D-1 sample via the implementation of a "slip-casting" method. In the case of the 3D-2 sample, the addition of carbon granules (ø1 mm and length of a few mm, added in a 10% wt. of the amount of the Ni-ferrite that was used in the mixture) aimed to facilitate formation of pores in the structure. In the case of the third sample (3D-3), the raw material that was used was the SHS synthesized Ni-ferrite that was only calcined at 1400 °C and the coarser particles were separated via sieving (Fischer Scientific sieve No. 40, sieve opening 425 μm).
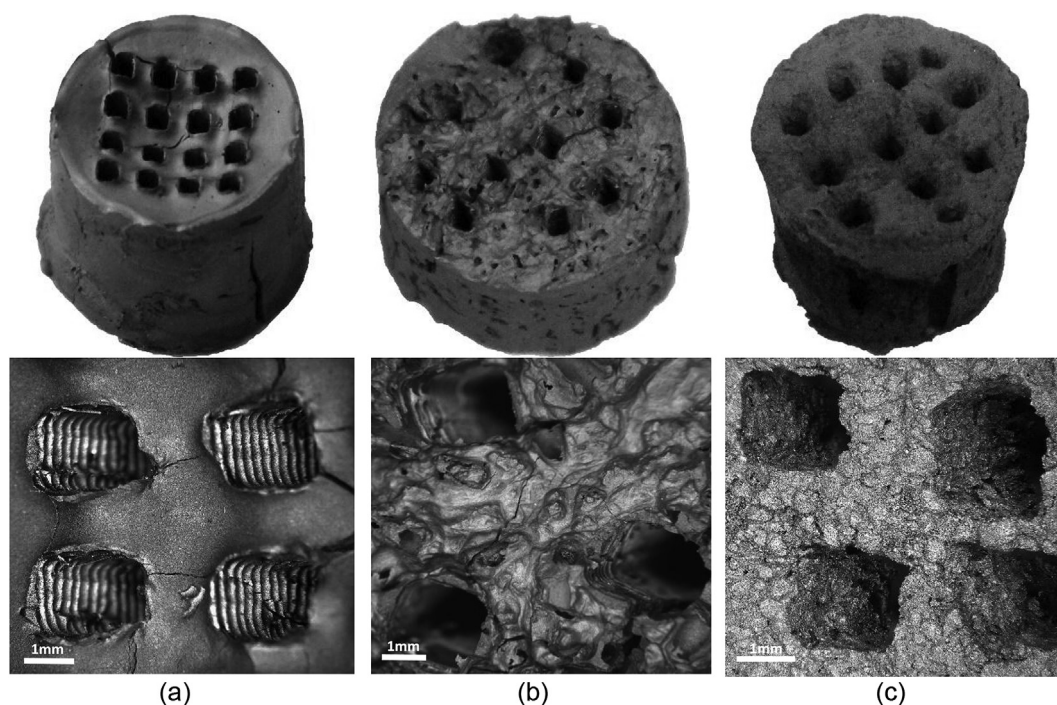

(a)   (b)   (c)

Fig. 9 – Ni-ferrite monolithic structures prepared from 3D-printed molds: (a) 3D-1, (b) 3D-2, (c) 3D-3, and the corresponding optical microscope images of their surface.
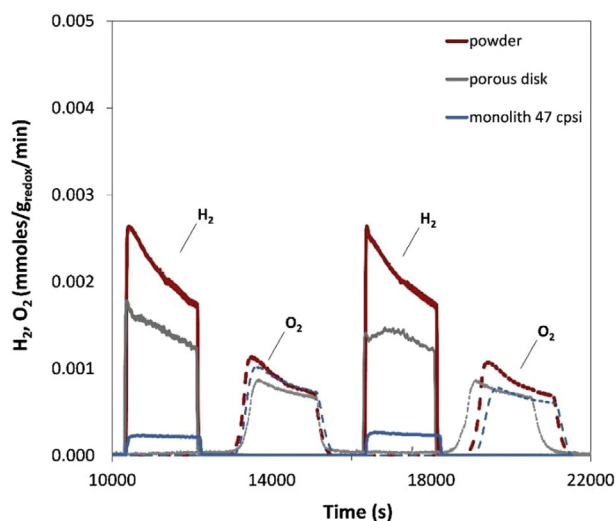
Fig. 10 – Typical H_2 and O_2 evolution curves during H_2O splitting (8% H_2O concentration at 1100 °C) and thermal reduction (at 1400 °C) on Ni-ferrite powder, porous disk and 47 cpsi extruded honeycomb monolith.

Fig. 12 – Comparison of hydrogen and oxygen evolution curves during the splitting and thermal reduction cycles on the 47 cpsi fresh sample and on the sample after 11 consecutive cycles.

All structures (Fig. 9) were stable after firing at 1400 °C, however the presence of some superficial cracks was observed mostly in the first two cases (3D-1 and 2). Further magnification on the surface of the monoliths shows the difference that is caused mainly due to the pre-treatment of the Ni-ferrite powder. The 3D-1 monolith has a very smooth surface that resembles the surface of the extruded monolith and is the result of the slip-casting technique in addition to the particle size distribution of the ferrite powder used as raw material, while the surface of 3D-2 has a more uneven morphology due to the addition of carbon granules in the initial paste, which were burnt during the calcination process. The third sample (3D-3) has an even more irregular surface that is induced from the coarser particles of the raw material due to the different
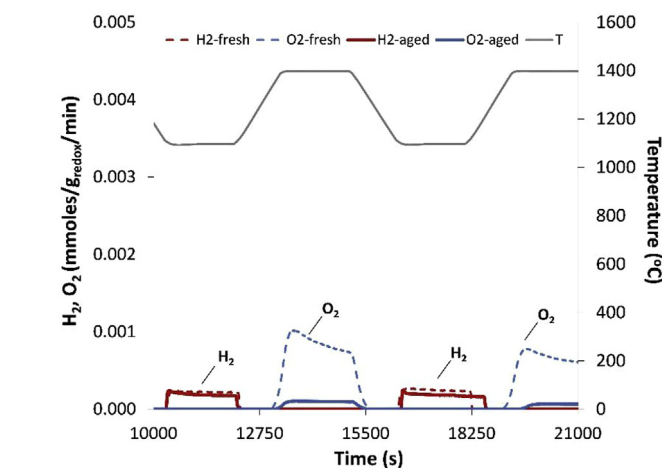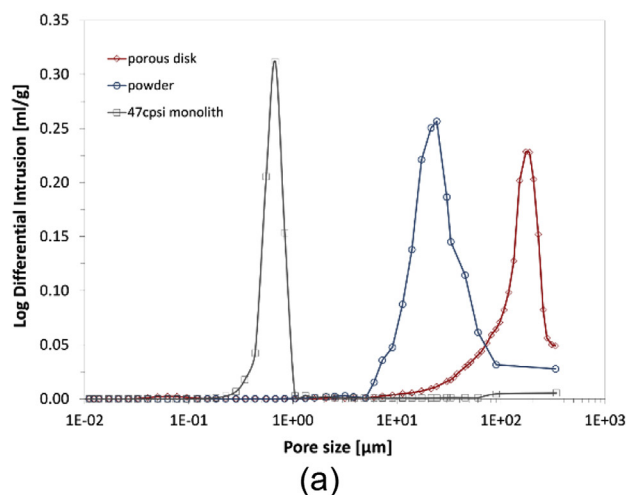
pre-treatment procedure of the Ni-ferrite powder (i.e. calcination of the SHS-Ni-ferrite powder and sieving).

Thermochemical redox cycles-water splitting

From powder to monolith

Fig. 10 shows the typical H_2 and O_2 evolution profiles for the case of the powder, the disk and the 47 cpsi extruded monolith (thick wall structure).

The different morphology of the H_2 and O_2 production curves makes evident the difference in the kinetics of the two reaction steps (the oxidation reaction is faster from the thermal reduction reaction, as observed in previous studies employing such non-stoichiometric two-step redox cycles) [e.g. Refs. [37–39]]. The decrease in the production of H_2, during the H_2O splitting step, indicates the extinction of the available sites that can receive the O-atoms from water at the
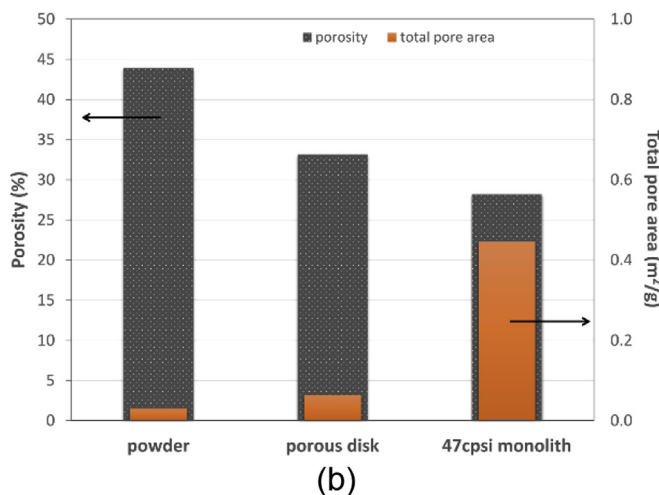

Fig. 11 – (a) Hg intrusion volume per g of sample as a function of pore diameter, (b) porosity and total pore area measured via Hg-porosimetry (within the range of pore diameters: 0.005–335 μm), for the case of the: powder bed, porous disk and 47 cpsi extruded monolith.
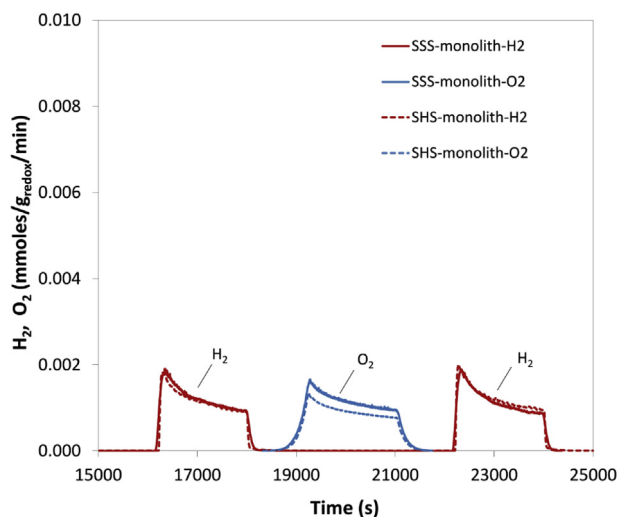
Fig. 13 – H$_2$ and O$_2$ evolution curves during water splitting (60% H$_2$O concentration at 1100 °C) and thermal reduction (at 1400 °C) on 150 cpsi Ni-ferrite extruded monolith from (a) NiO and Fe$_2$O$_3$ mixture of raw precursors and (b) SHS synthesized Ni-ferrite.

specific water pressure and temperature, while the decrease in the production of O$_2$, during the thermal reduction step, indicates the extend of the reduction/regeneration of the material that can be achieved at the specific temperature and step duration.

The amount of H$_2$ and O$_2$ produced during the oxidation and reduction steps is derived from the integral of the respective curves and is expressed in mmol/g$_{redox}$. The

activity of the 3 different formulations with respect to H$_2$ production follows the order of: powder > disk > monolith.

The H$_2$ evolution profiles vary significantly between the different structures. In the case of the Ni-ferrite powder there is a steeper decrease of H$_2$ concentration that flattens as the material formulation changes from disk to monolith, for low steam concentrations (8% H$_2$O in N$_2$). The profiles of O$_2$ evolution are similar among the different structures.

In all cases the H$_2$:O$_2$ ratio is different than the theoretical one (i.e. H$_2$:O$_2$ = 2). In the cases that the ratio value is close to the theoretical one, such as the case of the powder (H$_2$:O$_2$ = 2.15), the limiting factor is the thermal reduction step. Shifting from powder to the disk (H$_2$:O$_2$ = 1.7) and eventually to the honeycomb structure (H$_2$:O$_2$ = 0.3), the ratio becomes substantially lower than 2 due to the notably lower oxidation kinetics, but also due to the fact that for the structured bodies (monolith) the redox mass that is accessible to the reactants is actually proven to be much less than in the powder case.

The general idea was described in detail in Ref. [37]. At each scale (powder, disk, monolith), it could be considered that two distinct regions exist and participate in the redox scheme. The first region is in direct contact with the gas phase ("outer region") and the second one has no direct access to the gas phase ("inner region"). Both these regions can be considered to exist in all samples but to a different relative extent and depending on sample morphology (powder bed, porous disk, honeycomb monolith).

The "outer region" (surface) includes the pore structure that naturally can be considered to be completely filled with gas. Water splitting and regeneration reactions occur directly in this first region of the redox material. In the "inner region" oxygen atoms can move through the bulk towards the surface activated by oxygen vacancies.
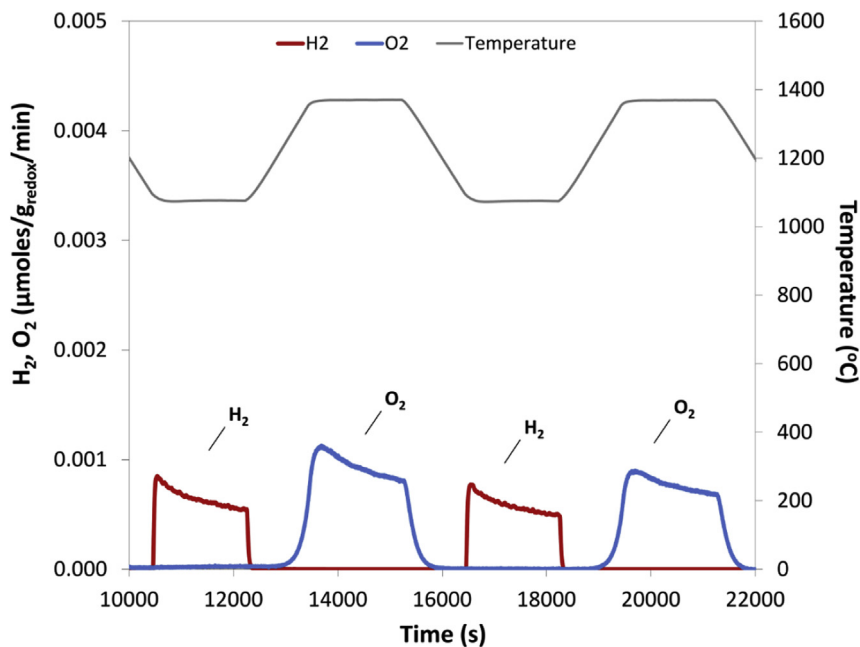
Fig. 14 – H$_2$ and O$_2$ evolution curves during water splitting and thermal reduction on Ni-ferrite 90 cpsi extruded monolith (3rd–4th cycle) (8% H$_2$O concentration).

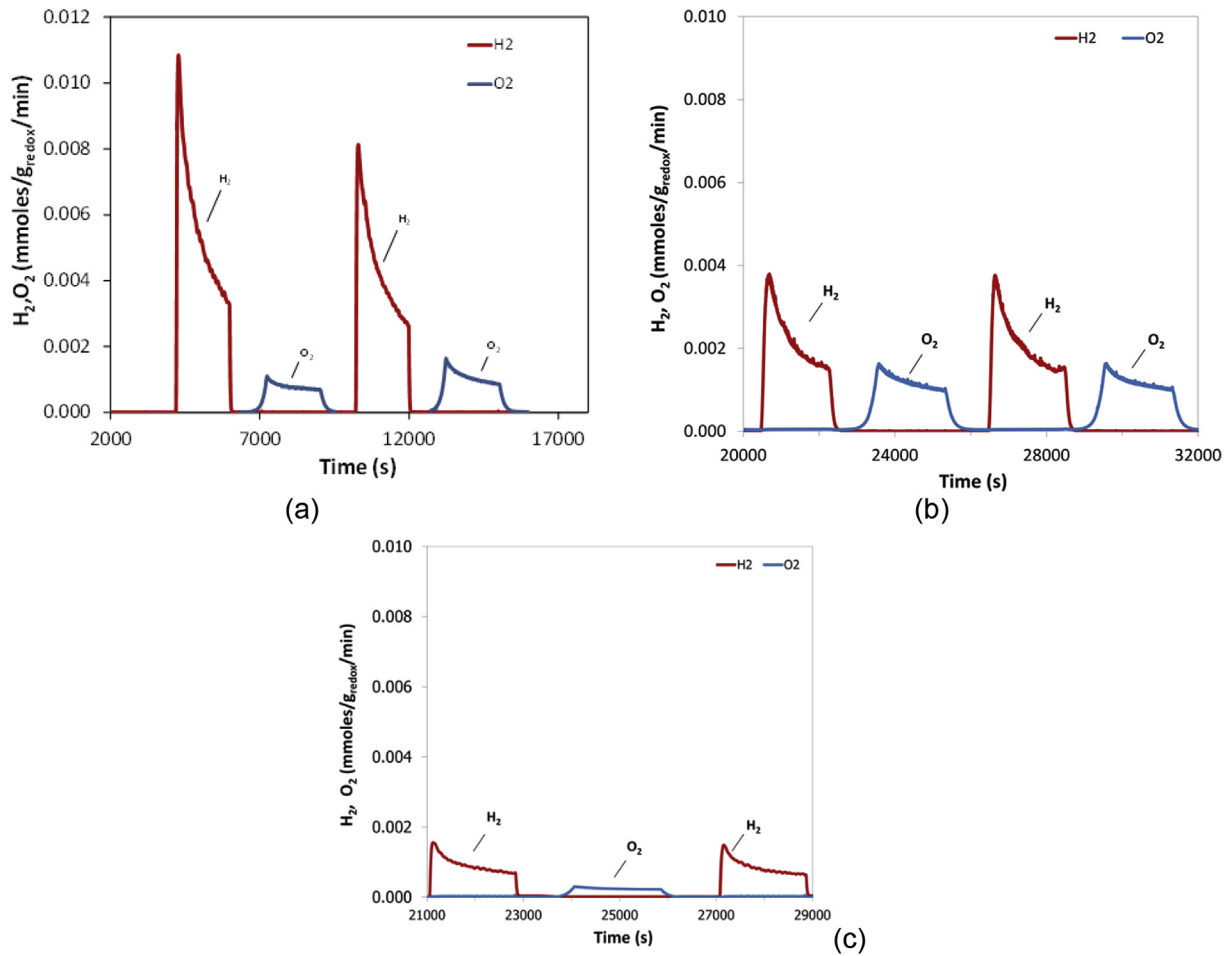**Fig. 15 – H₂ and O₂ evolution curves during water splitting and thermal reduction on (a) Ni-ferrite powder (1st–2nd cycle), (b) Ni-ferrite 90 cpsi (34th–35th cycle) and (c) 47 cpsi extruded monolith (12th–13th cycle) (60% H₂O concentration).**
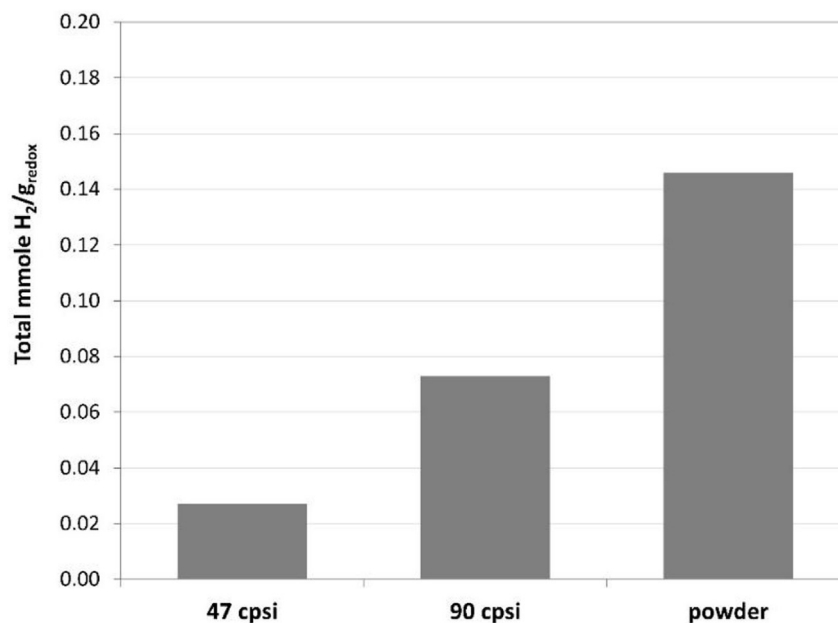

Fig. 16 – Comparison of the total H₂ yield between the two honeycomb monoliths with the different cell density and wall thickness and the powder (60% H₂O concentration).
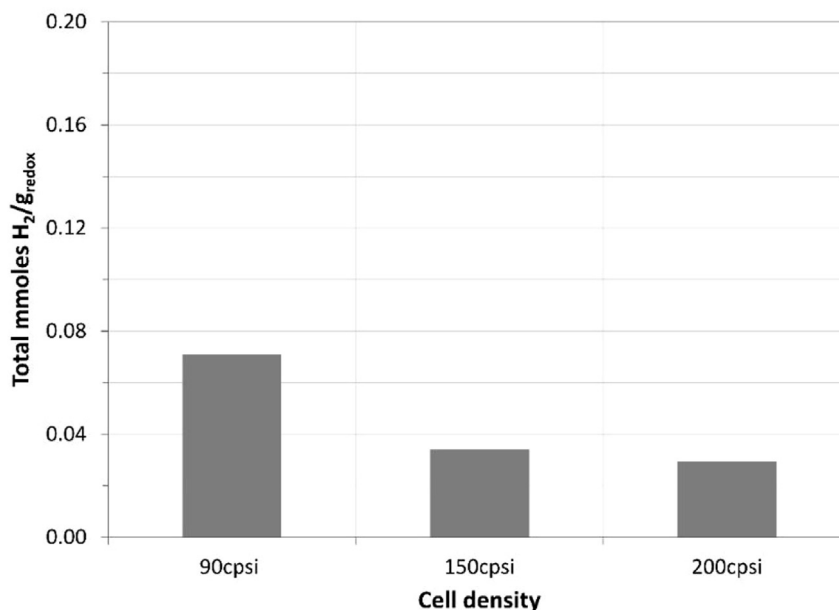
Fig. 17 – Total H_2 yield for the 3 honeycomb monolithic structures with different cell density and same wall thickness (60% H_2O concentration).
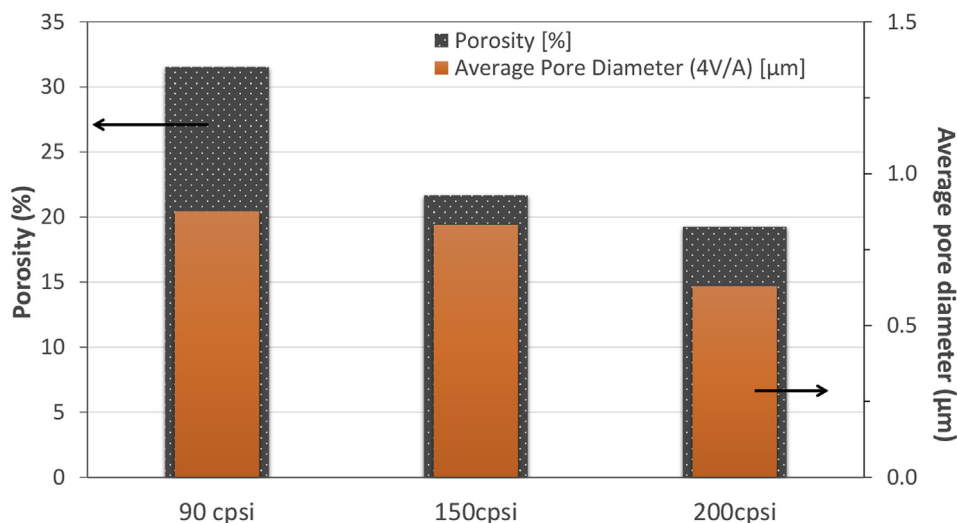

Fig. 18 – Porosity and average pore diameter for the 3 honeycomb monolithic structures with different cell density and same wall thickness (cpsi).

Therefore, this difference between O_2 and H_2 evolution of the various material scales could mainly originate from the fact that, in the case of the reduction step, both the "outer" and the "inner" regions participate in the exchange of O-atoms. On the contrary, in the case of water splitting, the "outer region" is the most active one since it is readily accessible by H_2O molecules, while, in order to exploit also the "inner region", pathways should be formed in the bulk of the material that would allow accessibility via diffusion mechanisms of sufficiently fast kinetics (e.g. a network of pores with increased connectivity).

In the case of the powder the particle grains form the external surface of the sample, therefore increasing, at a first step, the area that is accessible from H_2O molecules and consequently increasing the H_2 production. This is an indication of the effect of the morphology of the "outer region".

At the disk scale, since it is a highly porous structure, there is still appreciable surface area accessible to the flow but not as high as at the scale of the powder.

The porosity and pore size distribution of the samples was measured via gas adsorption analysis (BET measurement). In order to have a more representative result regarding the state of the samples during the redox reactions, the samples were additionally fired under N_2, since the redox cycles are conducted under inert atmosphere. In the case of the powder, a very low porosity and specific surface area was measured (0.3 m^2/g), while the porous disk and the extruded monolith gave no measurable results, indicating that these samples do
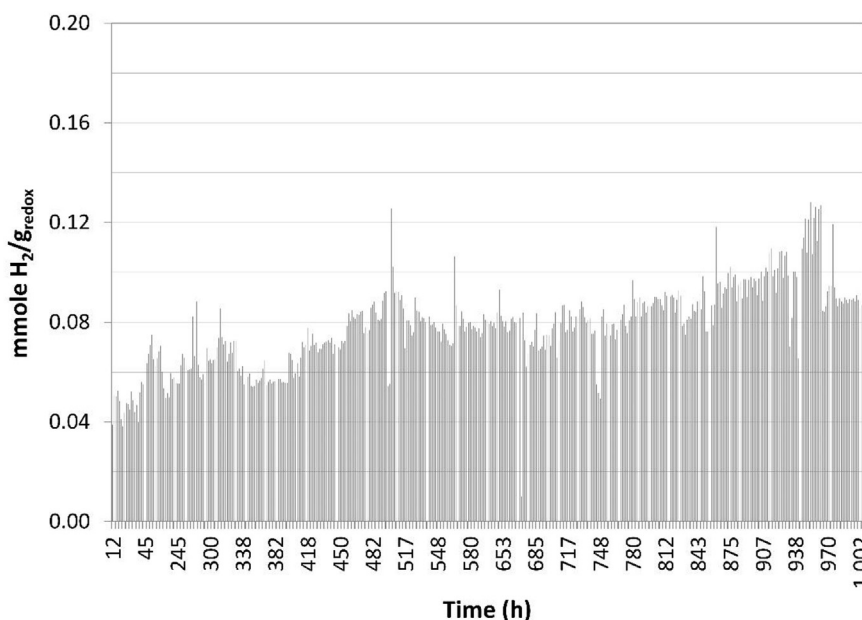
Fig. 19 – Total H_2 yield during multiple H_2O splitting cycles on Ni-ferrite 90 cpsi extruded monolith (60% H_2O concentration).

not have accessible pores in the range measured via gas adsorption (pore diameters <5 nm). Therefore, Hg-porosimetry was employed to cover a wider range of pore sizes (~5 nm–335 μm) that may be present in the samples. Contrary to the absence of pores recorded via nitrogen adsorption, Hg-porosimetry revealed in all cases the existence of larger pores that contribute to the samples with some additional active surface area.

Fig. 11(a) illustrates the Hg differential intrusion volume per g of sample as a function of pore size for the case of the powder, the porous disk and the 47 cpsi extruded monolith (all samples measured after adhesion firing under N_2). As expected the porous disk had substantially larger pores, as a
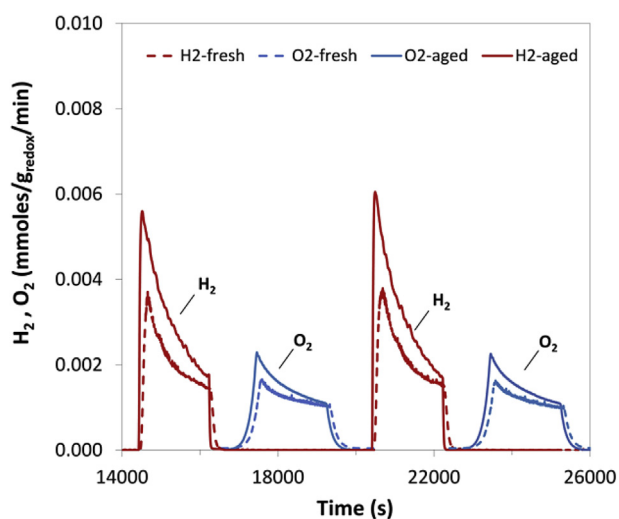

Fig. 20 – H_2 and O_2 evolution curves during water splitting and thermal reduction on Ni-ferrite 90 cpsi extruded monolith for the case of the fresh (34th–35th cycle) and the aged (600–601 cycle) (60% H_2O concentration).

result of the pore forming agent (carbon granules ø1 mm and length few mm) employed during its manufacturing process. From the graph it is also obvious that both the porous disk and the powder bed have a population of pores that lies above the 335 μm, which is the upper limit of the Hg-porosimeter. On the other hand, the extruded monolith had significantly smaller pores and narrower pore size distribution, which can be attributed to the high pressures that are applied during the extrusion process. The porosity of the samples also varies among the different structures. In the case of the powder and the porous disk, porosity was 43 and 33% respectively, while the porosity of the monolith was much lower (28%). The total pore area (m^2/g) of the samples, as expected, follows the exact reverse order with the extruded monolith, exhibiting the highest value (0.45 m^2/g) while the powder the lowest one (0.03 m^2/g).

The higher porosity of the powder, in combination with the large size of the pores, may explain the higher redox activity since it enables the flow to reach more active sites and thus enhances the contact of the gaseous reactants with the active material.

The performance of the porous disk is the closest one to the performance of the powder, with respect to water splitting activity. Although it has lower porosity (~23% lower than the powder), the even larger size of the pores, allows a higher degree of contact. This is reflected also in the redox activity of the disk compared to the powder (as depicted in Fig. 10).

The 47 cpsi extruded monolith is the most inaccessible structure, although the presence of honeycomb channels contributes positively to the surface area exposed to the reaction stream. Apparently, the extrusion process induces the formation of very small pores. Although the existence of small pore sizes contributes positively to the total pore area detected in the sample by Hg-porosimetry, however the majority of these pores is not accessible from the reactants flow.
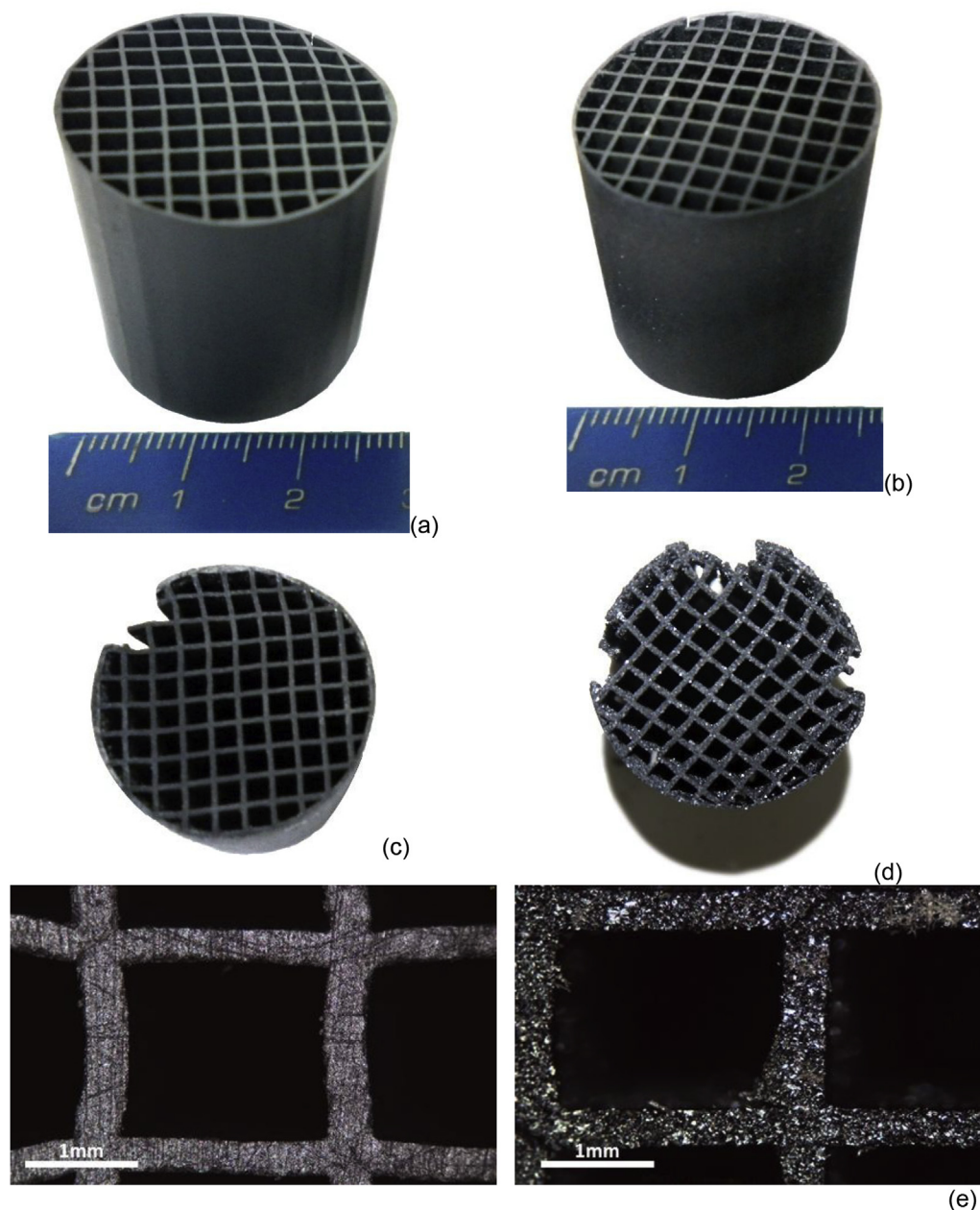
Fig. 21 – Ni-ferrite 90 cpsi extruded monolith (a) fresh, (b) after 70 h and (c) after 410 h and (d) after >1000 h of consecutive water splitting (1100 °C) and thermal reduction cycles (1400 °C). (e) Cross section of the channel viewed via an optical microscope (left: fresh, right: aged).

This explains also the very low $H_2:O_2$ ratio in the case of the 47 cpsi extruded monolith, since O_2 during the thermal reduction step evolves from the whole mass of the monolithic walls, while H_2 is the product of the reaction of H_2O with a much smaller part of the redox mass, naturally located near the surface of the channel wall. This means that only a small percentage of the oxygen vacancies formed during the thermal reduction step was subsequently covered by the oxygen from H_2O. Increasing the extend of reduction of the monolith (e.g. via consecutive cycles) does not increase further the H_2 yield of the structure, but eventually improves the $H_2:O_2$ ratio since the bulk O_2 of the material is exhausted and O_2 evolving during thermal reduction corresponds entirely to the oxygen

that was removed from H_2O during the preceding splitting step (from 28 mmol/g of O_2 recorded in the first cycles the oxygen evolution drops to 3 mmol/g of O_2 in the last cycles Fig. 12).

Extruded monoliths: effect of raw material
As described earlier in the text, two monoliths with the same geometrical characteristics (i.e. wall thickness and channel size, in the specific case the segments had a 150 cpsi cell density) starting from different raw material (i.e. from NiO and Fe_2O_3 reactants in one case (SSS-extruded) and from SHS synthesized Ni-ferrite in the other case (SHS-extruded)), were evaluated with respect to their redox activity. Both monoliths
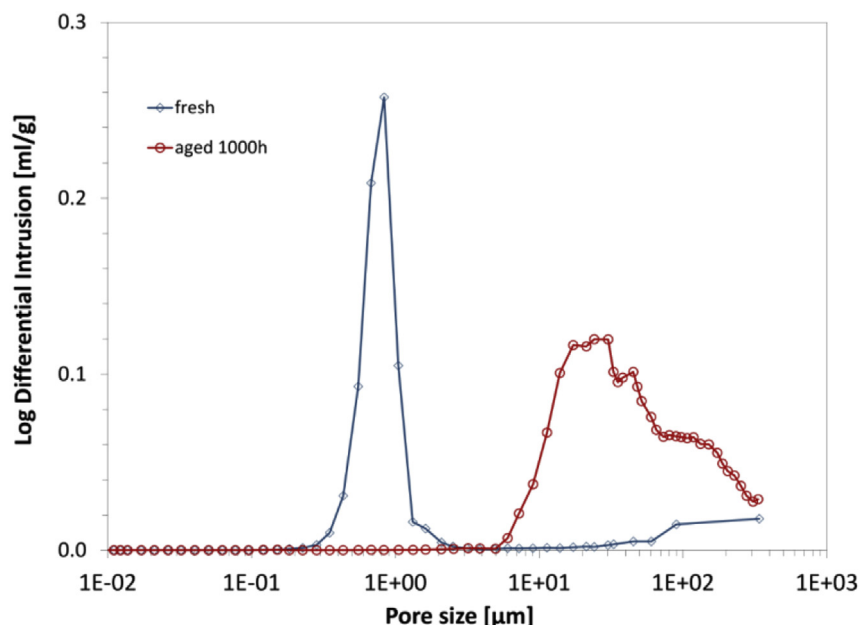
Fig. 22 — Pore size distribution measured via Hg-porosimetry for the case of fresh and 1000 h aged 90 cpsi extruded monolith.

had the same phase composition, as shown in (Fig. 5). From a previous work [36], it was observed that the Ni-ferrite powder synthesized via the SHS process had almost identical redox behavior — with respect to H_2O splitting — compared to the same material deriving from the conventional SSS route. Consequently, in the case of the monoliths the similarity in the phase composition was also projected to their redox activity.

Fig. 13 shows the H_2 and O_2 evolution profiles during the splitting and the thermal reduction steps respectively, for the two honeycomb monoliths. The H_2 yield (37.8 mmol H_2/g_{redox} for the "SSS-monolith" and 37.31 mmol H_2/g_{redox} for the "SHS-monolith") and $H_2:O_2$ ratio (0.92 and 1.07 respectively) were comparable, similarly to the behavior of the "SSS" and "SHS" Ni-ferrite in powder form [35]. The latter indicates that the SSS-extruded monolith could play the role of the "simulant" for the investigation of the effect of different geometric parameters (e.g. wall thickness, channel size) on the performance of the monolith. This was important since the extrusion process requires significant amounts of raw material (order of kgs) to produce the monolithic segments, which surpasses current work's laboratory scale manufacturing of the ferrite via the SHS route.

Therefore, the results that are discussed from this point on are based on honeycomb monoliths extruded from a stoichiometric mixture of the appropriate oxides (NiO and Fe_2O_3) in a first step and the subsequent formation of the Ni-ferrite on the monolithic structure at a second step, as described in the experimental section.

Extruded monoliths: effect of monolith geometry
Increasing the number of cells in the honeycomb monolith would have as a result the increase of the surface area exposed to the flow. Since as discussed earlier in Section From

powder to monolith, the "outer region" of the wall is the main part of the monolith that participates in the water splitting reaction, the decrease in the monolith's wall thickness, accompanied by a decrease in its channel size, or in other words the increase of cell density, would increase the surface area.

A Ni-ferrite monolith with higher cell density (90 cpsi) was assessed with respect to its H_2O splitting potential under the conditions described in the experimental section. The evolution profiles of H_2 and O_2 are depicted in Fig. 14 for the case of 8 vol% of H_2O.

Compared to the 47 cpsi monolith, the 90 cpsi appears to be substantially more active. The effect is more pronounced if it is taken into consideration the fact that the H_2 yield is expressed as a function of mass of redox material (i.e. mmol/g_{redox}/min). In the case of the 47 cpsi extruded monolith (thick wall structure), the amount of redox material per unit volume is larger in order to achieve the higher wall thickness (bulk density ~3 g/cm^3). On the other hand, the 90 cpsi monolith, has almost 2 times lower bulk density (bulk density ~1.66 g/cm^3). Expressing the evolution of H_2 as a function of the redox amount in the case of structured reactors is misleading, since not all amount of the redox material is exposed to the flow and therefore not all amount of the redox material is active during the splitting reaction. Moreover, since the solar receiver/reactors applied for the production of solar fuels are volumetric reactors, the most appropriate metric would be the volumetric yield. Therefore it can be deduced that, in the case of structured reactors, it is more representative to describe the yield of the reaction as a function of the volume or even the surface area of the structure and not per weight of redox material. However, still the monolith with the thinner walls and the higher cell density (90 cpsi) has a higher H_2 yield and has also the
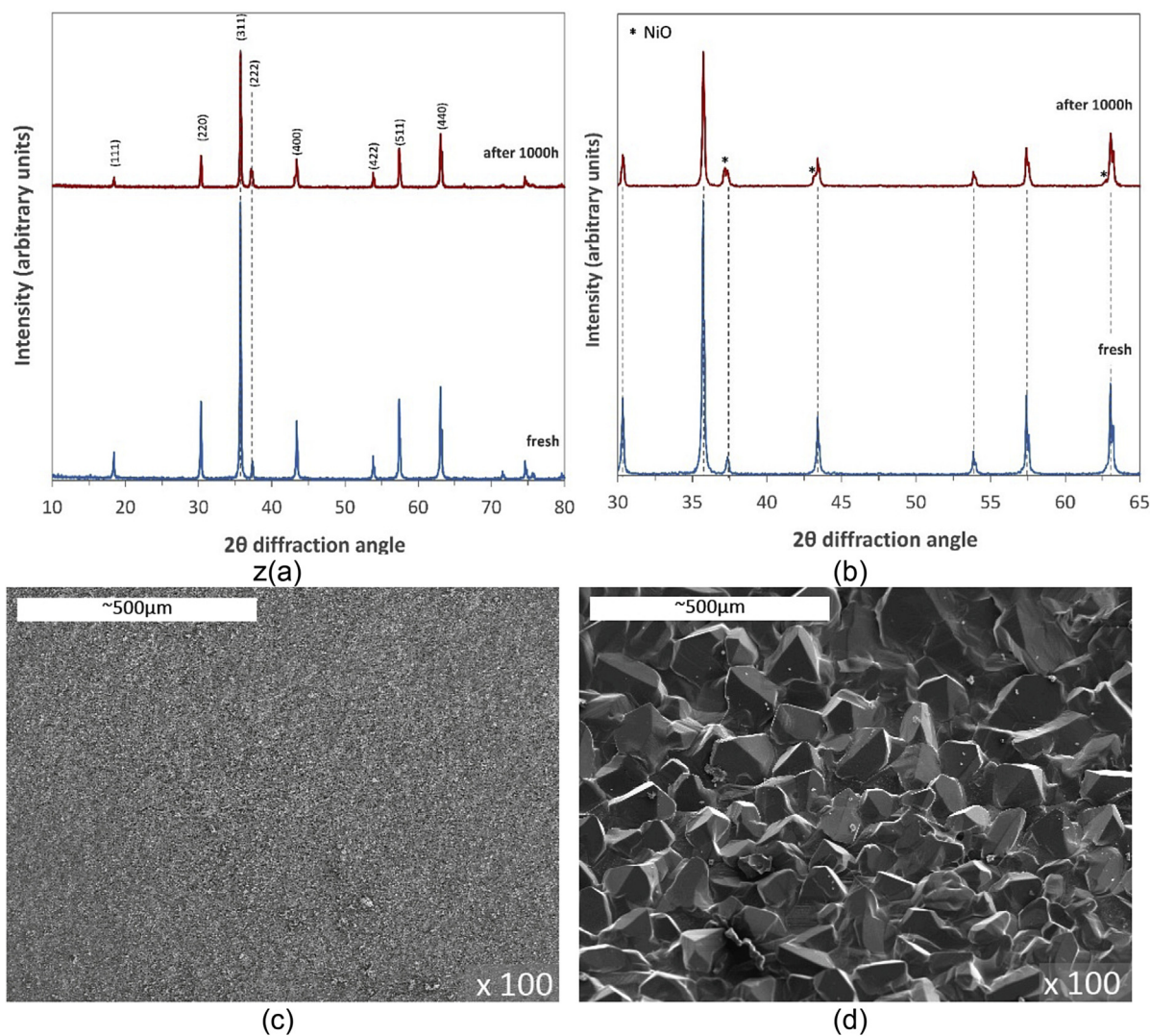
Fig. 23 — (a) XRD spectra of the fresh and the aged Ni-ferrite 90 cpsi monolith and (b) magnification of the spectrum to indicate the NiO peaks in the aged monolith. SEM analysis of the (c) fresh and (d) aged sample shows the significant grain growth on the monolith wall.

advantage of a lighter structure which is always important when dealing with constructions, especially at elevated heights and operating temperatures as in the case of solar towers.

Naturally, further increase of the H_2O concentration to 60 vol% resulted to the increase in H_2 production both in the powder ((a)) and in the honeycomb monolithic geometries (90 cpsi and 47 cpsi) (Fig. 15(b) and (c)).

Compared to the Ni-ferrite powder the honeycomb monolithic structures continue to have lower redox activity even under high steam concentration (60%). However, still the water splitting in the powder bed leads to higher yields. It is obvious that, via the increase of the cell density, the performance of honeycomb monoliths comes closer to that of the reference powder (Fig. 16).

Nevertheless, increasing further the cell density of the monoliths from 90 cpsi to 150 and 200 cpsi did not have the anticipated result in the performance of the structure (i.e. increase of cell density → increase of redox activity). Actually

the 90 cpsi monolith appears to have the highest H_2 yield compared to the monoliths with higher cell density and the same wall thickness (Fig. 17). This performance may be related to the lower porosity of the monoliths and the tendency for even smaller pores observed in the segments with the higher cell density which is related to the extrusion process (Fig. 18). Consequently, lower wall porosity reduces the accessibility of the flow to the redox material and therefore, a higher amount of material remains unexploited.

Extruded monoliths: durability assessment
From the evaluation of the different extruded honeycombs, the 90 cpsi monolith proved to have the best performance. Therefore, this particular structure was chosen for further durability assessment under multiple water splitting and thermal reduction cycles. Fig. 19 illustrates the calculated total yield of H_2 during approximately 600 consecutive splitting (60 vol% H_2O concentration) and thermal reduction cycles, corresponding to >1000 h exposure at temperatures from
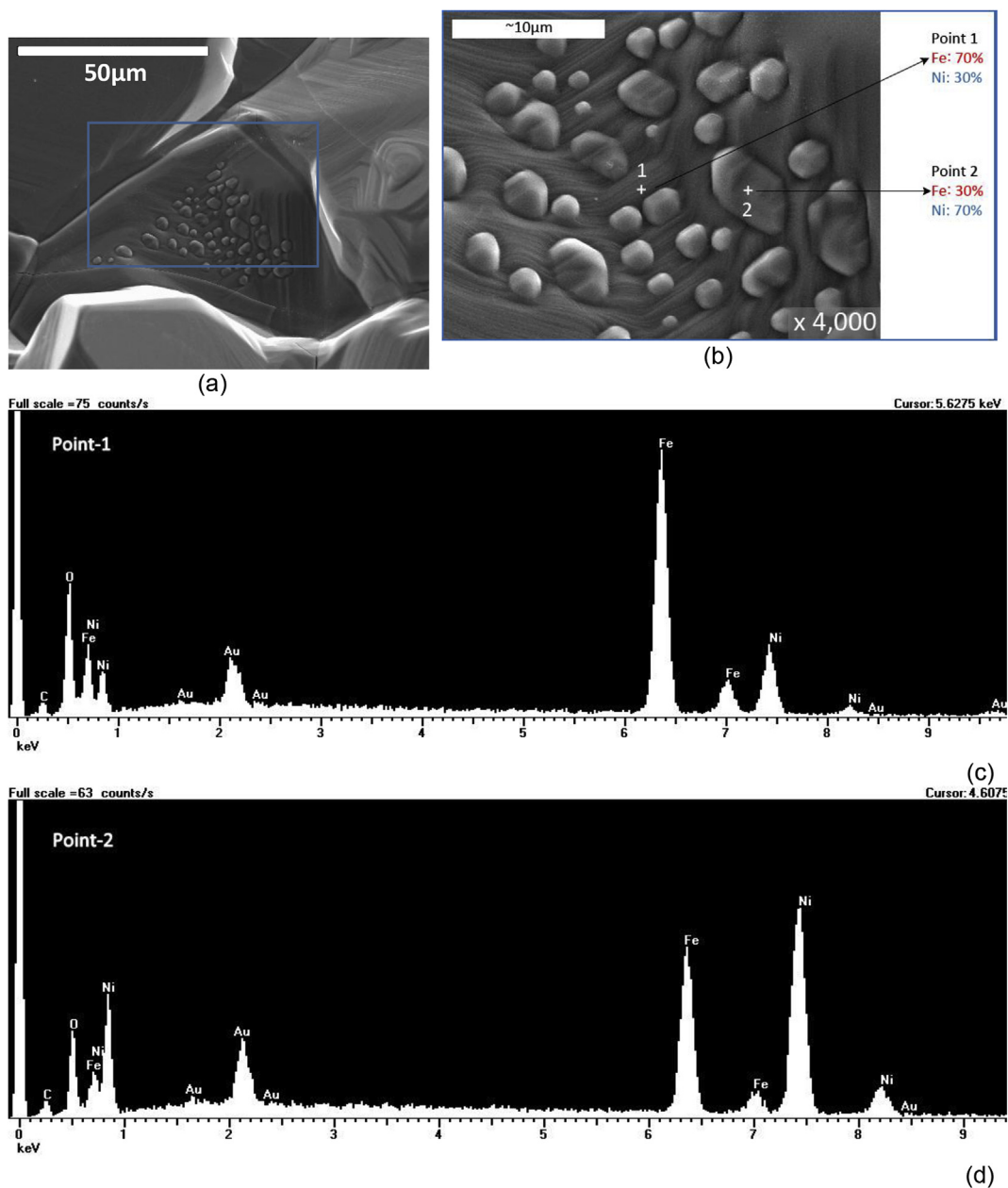
Fig. 24 — SEM images of the aged Ni-ferrite monolith (a) magnification ×1000 times and (b) higher magnification ×4000 times and (c, d) EDS spectra of Points 1 and 2 marked upon image (b).

1100 to 1400 °C. H_2 production appeared to be more or less stable, with a slight increase in the yield from start-to-end of the evaluation (Fig. 20).

The improved activity of the aged monolith could be an effect of its sintering that alters its structural characteristics (e.g. shrinkage, formation of cracks etc.), due to the prolonged exposure time at the high temperatures of the process (Fig. 21). These structural changes cause exposure of new surfaces that were previously inaccessible from the flow. The result is an increase in the H_2 yield. This performance is in contrast to that of the powder. Although the powder has a higher yield compared to the structured monolith, the sintering that it suffers during consecutive splitting and regeneration cycles affects its performance, as discussed in a

previous work [30]. In Ref. [30], the effect of sintering of the powder was investigated by assessing the redox activity of the powder in the fresh state, after one cyclic operation, followed by grinding of the sample between the cycles in order to restore its active surface, and evaluating again its performance. The result was that grinding of the powder after use improved its activity. Therefore a reactor consisting of structured bodies would have the advantage of a more or less stable activity, compared to a powder fixed bed reactor which would require "drastic intervention" in order to alleviate the effects of consecutive high temperature exposure.

By focusing on the microstructure of the monolith via optical microscopy (Fig. 21(e)) the changes afflicted on the
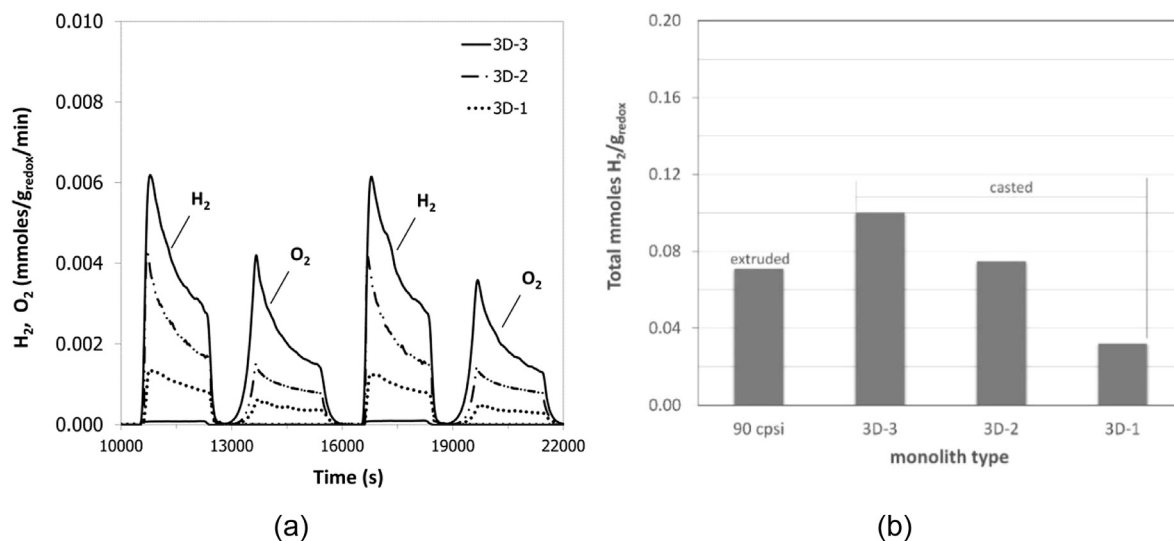
Fig. 25 – (a) H_2 and O_2 evolution curves during water splitting and thermal reduction (3rd–4th cycle) on the Ni-ferrite 3D-1, 2 and 3 monoliths, and (b) total H_2 yield of the cast monoliths compared to the extruded monolith with the best performance (60% H_2O concentration).

channel walls due to the long-term exposure at high temperatures are revealed.

Hg-porosimetry performed on the aged monolith quantifies the changes optically observed. As illustrated in (Fig. 22), there was significant increase in the diameter of the pores in the aged sample. In addition, the morphology of the pore size distribution curve of the aged monolith is much wider than the well determined narrow distribution of the fresh monolith.

The XRD comparison spectra of the fresh material and the aged monolith – i.e. after 1000 h of consecutive water splitting and thermal reduction cycles – showed a small, yet clearly detectable, change in the phase composition. The aged structure maintained the Ni–Fe-spinel structure. However, the spectrum shifted, from $Ni_{1.25}Fe_{1.85}O_4$ to $NiFe_2O_4$. In addition, the characteristic peaks of NiO appeared in the spectrum at low intensities.

SEM analysis of the walls of the extruded monolith prior and post the long-term durability evaluation, revealed significant increase of the grain size of the material (Fig. 23). At higher magnification, apart from the observed patterns of grain growth, there were also regions on the surface of the grains of the monolith wall that varied in composition, as identified by EDS analysis (Fig. 24). EDS spectra taken from two specific points on a grain (Point-1 and Point-2) showed differences in the Fe:Ni ratio. Point-1 (grain surface) has the typical Fe:Ni = 70:30 ratio of the $NiFe_2O_4$ composition, while Point-2 (segregated particle) revealed considerably higher content in Ni (Fe:Ni = 30:70), which is attributed to the excess Ni that separated in the form of NiO on the aged monolith, that was also confirmed via XRD analysis.

3D-print cast monoliths: redox assessment
The preliminary assessment of the structures shaped via 3D-printed casts, with respect to their redox activity, showed that they are indeed active water splitters. All samples were

evaluated under 60% H_2O concentration in N_2 and according to the general protocol described in the experimental section. Fig. 25 illustrates the H_2 and O_2 evolution curves during water splitting and thermal reduction on the three structures (two representative cycles). As it can be observed, 3D-3 has the highest H_2 yield while the 3D-1 structure has the lowest. Such differences in the performance are attributed to the notable differences in of the monoliths' surface morphologies.

When comparing the performance of the cast monoliths, in terms of total mmol of H_2/g_{redox}, with the best performing Ni-ferrite extruded monolith (i.e. 90 cpsi extruded monolith), it can be observed that the cast monoliths show a promising potential (Fig. 25(b)). The 3D-3 structure exhibited a hydrogen yield ~30% higher than that measured in the case of the 90-cpsi extruded honeycomb.

In general, there is the need for further evaluation of the 3D-cast structures at similar time scales as that of the extruded monolith to assess their long-term potential. In principle, there is room for further enhancement of the redox activity of the 3D-cast monoliths via alteration of their porosity (e.g. addition of pore forming agents to increase the porosity and the wall surface roughness) as well as their geometric characteristics (e.g. higher number of channels, thinner walls, wall-flow monoliths with the prerequisite of high wall permeability to allow the flow to pass through the wall without a high pressure drop penalty etc.).

Conclusions

In the process of investigating the possibility to manufacture efficient structured reactors, consisting entirely of the redox material (Ni-ferrite), for solar thermochemical redox reactions (e.g. H_2O or CO_2 splitting), several approaches have been investigated. All structures were active water splitters, however, as expected, they were inferior in the H_2 yield compared

to the performance of the plain Ni-ferrite powder. Nevertheless, appreciable performance enhancement can be achieved by modifying key structural characteristics, in order to induce porosity formation by addition of pore forming agents in the initial raw material mixture and ultimately increase the accessibility of the gaseous reactants to the active sites of the material.

Future work will focus on further evaluation of the 3D-cast structures as already mentioned in the previous section. In addition, the investigation of CO_2 splitting and co-feeding of H_2O and CO_2 on structured bodies, for the potential production of solar fuels, is of high interest. Other candidate materials and combinations thereof (e.g. CeZr-mixed oxides) that appear promising for H_2O and CO_2 splitting [13] will be also investigated for their potential in the formation of structured monolithic bodies.

Acknowledgements

REFERENCES

[1] Funk JE. Thermochemical hydrogen production: past and present. Int J Hydrogen Energy 2001;26(3):185—90.

[2] Carty RH, Mazumder MM, Schreider JD, Panborn JB. Thermochemical hydrogen production, GRI-80/0023, vols. 1—4. Chicago, IL: Gas Research Institute for the Institute of Gas Technology; 1981. p. 1981.

[3] Mcquillan BW, Brown LC, Besenbruch GE, Tolman R, Cramer T, Russ BE, et al. High efficiency generation of hydrogen fuels using solar thermal-chemical splitting of water (solar thermo-chemical splitting for H_2), Las Vegas. 2010.

[4] Kodama T, Gokon N. Thermochemical cycles for high-temperature solar hydrogen production. Chem Rev 2007;107(10):4048—77.

[5] Steinfeld A. Solar thermochemical production of hydrogen — a review. Sol Energy 2005;78:603—15.

[6] Abanades S, Charvin P, Flamant G, Neveu P. Screening of water-splitting thermochemical cycles potentially attractive for hydrogen production by concentrated solar energy. Energy 2006;31:2805—22.

[7] Perkins C, Weimer AW. Likely near-term solar-thermal water splitting technologies. Int J Hydrogen Energy 2004;29:1587—99.

[8] Palumbo RD, Fletcher EA. High temperature solar electrothermal processing-III. Zinc from zinc oxide at 1200—1675 K using a non-consumable anode. Energy 1988;13(4):319—32.

[9] Scheffe JR, Li J, Weimer AW. A spinel ferrite/hercynite water-splitting redox cycle. Int J Hydrogen Energy 2010;35(8):3333—40.

[10] McDaniel AH, Ambrosini A, Coker EN, Miller JE, Chueh WC, O'Hayre R, et al. Nonstoichiometric perovskite oxides for solar thermochemical H_2 and CO production. Energy Procedia 2013;49:2009—18.

[11] Kuhn M, Bishop SR, Rupp JLM, Tuller HL. Structural characterization and oxygen nonstoichiometry of ceria-zirconia ($Ce_{1-x}Zr_xO_{2-\delta}$) solid solutions. Acta Mater 2013;61(11):4277—88.

[12] Lorentzou S, Karagiannakis G, Pagkoura C, Zygogianni A, Konstandopoulos AG. Thermochemical CO_2 and CO_2/H_2O splitting over $NiFe_2O_4$ for solar fuels synthesis. Energy Procedia 2013;49:1999—2008.

[13] Lorentzou S, Karagiannakis G, Dimitrakis D, Pagkoura C, Zygogianni A, Konstandopoulos AG. Thermochemical redox cycles over Ce-based oxides. Energy Procedia 2015;69:1800—9.

[14] Gokon N, Takahashi S, Yamamoto H, Kodama T. Thermochemical two-step water-splitting reactor with internally circulating fluidized bed for thermal reduction of ferrite particles. Int J Hydrogen Energy 2008;33(9):2189—99.

[15] Loutzenhiser PG, Meier A, Gstoehl D, Steinfeld A. CO_2 splitting via the solar thermochemical cycle based on Zn/ZnO redox reactions. In: Advances in CO_2 conversion and utilization. ACS Symposium Series. American Chemical Society; 2010. p. 3—25.

[16] Furler P, Scheffe J, Gorbar M, Moes L, Vogt U, Steinfeld A. Solar thermochemical CO_2 splitting utilizing a reticulated porous ceria redox system. Energy & Fuels 2012;26(11):7051—9.

[17] Chueh WC, Falter C, Abbott M, Scipio D, Furler P, Haile SM, et al. High-flux solar-driven thermochemical dissociation of CO_2 and H_2O using nonstoichiometric ceria. Science 2010;330(6012):1797—801.

[18] Agrafiotis CC, Roeb M, Konstandopoulos AG, Nalbandian L, Zaspalis VT, Sattler C, et al. Solar water splitting for hydrogen production with monolithic reactors. Sol Energy 2005;79(4):409—21.

[19] Roeb M, Monnerie N, Schmitz M, Sattler C, Konstandopoulos AG, Agrafiotis CC, et al. Thermo-chemical production of hydrogen from water by metal oxides fixed on ceramic substrates. In: Proceedings of the 16th World Hydrogen Energy Conference, Lyon, France, June, vol. 16. WHEC; 2006. p. 1—12.

[20] Säck JP, Breuer S, Cotelli P, Houaijia A, Lange M, Wullenkord M, et al. High temperature hydrogen production: design of a 750 KW demonstration plant for a two step thermochemical cycle. Sol Energy 2016;135:232—41.

[21] Kodama T, Gokon N, Yamamoto R. Thermochemical two-step water splitting by ZrO_2-supported $Ni_xFe_{3-x}O_4$ for solar hydrogen production. Sol Energy 2008;82(1):73—9.

[22] Miller JE, Allendorf MD, Diver RB, Evans LR, Siegel NP, Stuecker JN. Metal oxide composites and structures for ultra-high temperature solar thermochemical cycles. J Mater Sci 2008;43(14):4714—28.

[23] Walker LS, Miller JE, Hilmas GE, Evans LR, Corral EL. Coextrusion of zirconia—iron oxide honeycomb substrates for solar-based thermochemical generation of carbon monoxide for renewable fuels. Energy & Fuels 2012;26(1):712—21.

[24] Gokon N, Kodama T, Imaizumi N, Umeda J, Seo T. Ferrite/zirconia-coated foam device prepared by spin coating for solar demonstration of thermochemical water-splitting. Int J Hydrogen Energy 2011;36(3):2014—28.

[25] Agrafiotis CC, Roeb M, Sattler C. A review on solar thermal syngas production via redox pair-based water/carbon dioxide splitting thermochemical cycles. Renew Sustain Energy Rev 2015;42:254—85.

[26] McDaniel AH. Renewable energy carriers derived from concentrating solar power and nonstoichiometric oxides. Curr Opin Green Sustain Chem 2017;4:37—43.

[27] Aoki H, Kaneko H, Hasegawa N, Ishihara H, Takahashi Y, Suzuki A, et al. Two-step water splitting with Ni-Ferrite

system for solar H_2 production using concentrated solar radiation. In: ASME 2004 International Solar Energy Conference. Portland, Oregon, USA; 2004. p. 515–7.

[28] Gokon N, Mataga T, Kondo N, Kodama T. Thermochemical two-step water splitting by internally circulating fluidized bed of $NiFe_2O_4$ particles: successive reaction of thermal-reduction and water-decomposition steps. Int J Hydrogen Energy 2011;36(8):4757–67.

[29] Dimitrakis DA, Tsongidis NI, Konstandopoulos AG. Reduction enthalpy and charge distribution of substituted ferrites and doped ceria for thermochemical water and carbon dioxide splitting with DFT+U. Phys Chem Chem Phys 2016;18(34):23587–95.

[30] Agrafiotis CC, Pagkoura C, Zygogianni A, Karagiannakis G, Kostoglou M, Konstandopoulos AG. Hydrogen production via solar-aided water splitting thermochemical cycles: combustion synthesis and preliminary evaluation of spinel redox-pair materials. Int J Hydrogen Energy 2012;37(11):8964–80.

[31] Pagkoura C, Karagiannakis G, Zygogianni A, Lorentzou S, Kostoglou M, Konstandopoulos AG, et al. Cobalt oxide based structured bodies as redox thermochemical heat storage medium for future CSP plants. Sol Energy 2014;108:146–63.

[32] Karagiannakis G, Pagkoura C, Zygogianni A, Lorentzou S, Konstandopoulos AG. Monolithic ceramic redox materials for thermochemical heat storage applications in CSP plants. Energy Procedia 2014;49:820–9.

[33] Addiego WP, Liu W, Boger T. Iron oxide-based honeycomb catalysts for the dehydrogenation of ethylbenzene to styrene. Catal Today 2001;69(1–4):25–31.

[34] Karagiannakis G, Pagkoura C, Halevas E, Baltzopoulou P, Konstandopoulos AG. Cobalt/cobaltous oxide based honeycombs for thermochemical heat storage in future concentrated solar power installations: multi-cyclic assessment and semi-quantitative heat effects estimations. Sol Energy 2016;133:394–407.

[35] Pagkoura C, Karagiannakis G, Zygogianni A, Lorentzou S, Konstandopoulos AG. Cobalt oxide based honeycombs as reactors/heat exchangers for redox thermochemical heat storage in future CSP plants. Energy Procedia 2015;69:978–87.

[36] Agrafiotis CC, Zygogianni A, Pagkoura C, Kostoglou M, Konstandopoulos AG. Hydrogen production via solar-aided water splitting thermochemical cycles with nickel ferrite: experiments and modeling. AIChE J 2013;59(4):1213–25.

[37] Kostoglou M, Lorentzou S, Konstandopoulos AG. Improved kinetic model for water splitting thermochemical cycles using nickel ferrite. Int J Hydrogen Energy 2014;39(12):6317–27.

[38] Neises M, Roeb M, Schmücker M, Sattler C, Pitz-Paal R. Kinetic investigations of the hydrogen production step of a thermochemical cycle using mixed iron oxides coated on ceramic substrates. Int J Energy Res 2009;34(8):651–61.

[39] Go KS, Son SR, Kim SD. Reaction kinetics of reduction and oxidation of metal oxides for hydrogen production. Int J Hydrogen Energy 2008;33(21):5986–95.